JOURNAL OF GUIDANCE, CONTROL, AND DYNAMICS
Vol. 25, No. 1, January–February 2002

Attitude Estimation for a Flexible Spacecraft in an Unstable Spin

Mark L. Psiaki,* Eric M. Klatt,† Paul M. Kintner Jr.,‡ and Steven P. Powell§
Cornell University, Ithaca, New York 14853-7501

An attitude reconstruction algorithm has been developed for a flexible sounding rocket whose spin vector nutates unstably about its minor inertia axis. The attitude estimates are needed for postflight analysis of the rocket's science data. An additional goal of the work is to show that a flexible-body model can be used in a Kalman filter or in a smoother. The attitude is estimated using a smoother whose dynamic model includes a main rigid body and a pair of elastic booms. Boom flexure is the principal cause of nutation instability. Boom bending is modeled by a Markov process, but the laws of mechanics are used to determine its influence on the attitude dynamics. This smoother achieves a better attitude estimation accuracy than can be achieved using a rigid-body model. The peak attitude error is estimated to be 4 deg, and the principal error source seems to be the limited accuracy of the rocket's attitude sensors.

I. Introduction

THIS work deals with the postflight attitude determination for a sounding rocket mission, the Cleft Accelerated Plasma Experimental Rocket (CAPER). CAPER was launched from the Andoya Rocket Range in Norway in January 1999. Its flight lasted slightly longer than 1200 s and reached an apogee altitude of 1360 km. The goal of this mission was to study the behavior of the ionosphere during auroral events. Attitude information is needed to transform CAPER's measurements of electric field components into geodetic coordinates. An attitude accuracy of from 2 to 4 deg is considered acceptable for the mission.

From an attitude determination standpoint, the important characteristics of the CAPER sounding rocket were as follows: Its attitude sensors were a vector sun sensor with a slit field of view, a fixed-head horizon crossing indicator (HCI), and a three-axis magnetometer that was mounted on a short boom. The rocket's attitude was passively spin stabilized with the nominal spin vector directed along its minor inertia axis. CAPER deployed several booms after exit from the atmosphere and after the final stage motor burn. The longest of these were two flexible 3-m booms that deployed perpendicular to the nominal spin axis and in opposite directions from each other. A schematic diagram of this configuration appears in Fig. 1.

Minor-axis spin stabilization is often used in sounding rocket experiments. Near the dawn of the space age, the Explorer-1 mission demonstrated that such a configuration has an unstable nutation mode due to energy dissipation in the flexible booms.[1] In many sounding rocket experiments it is acceptable for the nutation amplitude to grow as long as the resultant coning half-angle does not become too large by the end of the flight.

There are two major challenges in doing postflight attitude determination for CAPER. The first is the lack of rate-gyro data. This challenge dictates the use of an Eulerian dynamics model to propagate the attitude and rates between measurement sample times. The model becomes especially important toward the end of the flight, when only magnetometer data are available. The attitude estimate in rotation about the magnetic field vector is based solely on dynamic model propagation during this phase, and model inaccuracy will lead directly to attitude inaccuracy. The second major challenge springs from the first: The rocket's attitude dynamics model contains two sources of significant uncertainty. One is error in the prelaunch reported values of the moments and products of inertia. The other is bending motion of the booms.

There is a significant body of research that is related to this attitude determination problem. A number of studies have been made of the dynamics and stability of nonrigid spinning spacecraft, for example, see Ref. 2. They describe how dissipative flexible-body motions can cause nutation instability. Such studies are relevant to the development of a dynamic model for use in CAPER's attitude determination smoother.

Other relevant works deal with the general problem of spacecraft attitude determination. References 3–7 are examples of this type of work. They all employ Kalman filters in one form or another to estimate attitude based on a time series of measurements. Traditional filters, which propagate the attitude using rate gyros to avoid the use of uncertain dynamic models are discussed in Refs. 3 and 4. In Refs. 5–7, a newer breed of attitude determination filters is employed that do not use rate gyros. They explicitly include the attitude rates in the filter state and use Euler's equations to propagate the estimates of these states.

The current work extends the dynamic modeling ability of the newer filter/smoother design approach. Extensions are needed because of CAPER's instability. In Refs. 5–7, stable systems that experienced only small perturbations from a nominal state are dealt with. CAPER had a nutational instability that caused its coning half-angle to grow from 20 deg at the beginning of the flight to over 75 deg at the end. Therefore, its attitude reconstruction smoother needs a dynamic model that is accurate over a large portion of the state space.

One new feature of the CAPER smoother is that its dynamics model explicitly includes flexible-body effects. The filters of Refs. 5–7 all used rigid-body models. A spacecraft that had significant flexible-body motions due to launch damage is dealt with in Ref. 7, but those motions are approximated by using random-walk torques to perturb a rigid-body model. Unfortunately, the Ref. 7 approach works poorly for CAPER.

Another new feature of the CAPER smoother is that it explicitly estimates five of the six inertia parameters of the main rigid part of the spacecraft. The sixth parameter is not observable. Estimation of these inertia matrix elements improves the fidelity of the dynamic model over the wide range of spin states that occurred during the CAPER mission.

This paper uses a smoother to estimate CAPER's attitude because its task is to perform attitude reconstruction. Nevertheless, its main contributions are equally applicable to the real-time filtering case because of the close link between smoothing and Kalman filtering.

This paper's methods and findings are presented in two main sections. Section II describes the attitude reconstruction smoother. Section III presents the attitude determination results that have been

---

Received 23 March 2000; revision received 8 June 2001; accepted for publication 22 July 2001.

*Associate Professor, Sibley School of Mechanical and Aerospace Engineering. Associate Fellow AIAA.

†Graduate Student, School of Electrical Engineering.

‡Professor, School of Electrical Engineering.

§Research Support Specialist, School of Electrical Engineering.

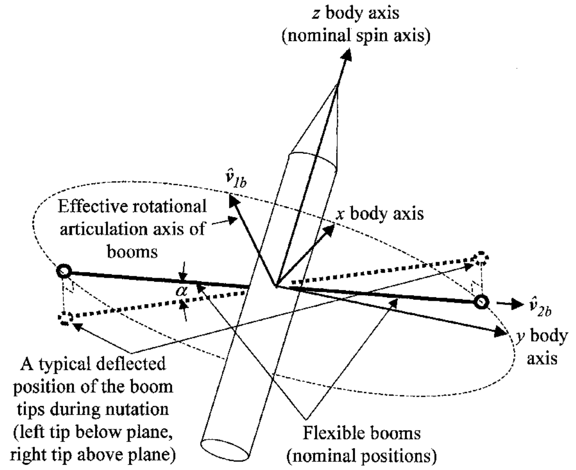

Fig. 1 CAPER sounding rocket configuration.

obtained using this smoother. Section III also compares these results with those of a Ref. 7 type smoother. Section IV summarizes the main conclusions.

II. Smoother Design

A. General Smoother Problem Statement

A sampled data square root information filter/smoother (SRIF/S) has been chosen as the means of reconstructing CAPER's attitude time history. It is an extension to the nonlinear case of the covariance smoother of Ref. 8. This smoother starts with a forward SRIF filtering pass and follows it with a backward covariance smoother pass. The extended algorithm is described in Ref. 7. It approximately solves a problem of the following form:

Find

$$\boldsymbol{x}_j \text{ and } \boldsymbol{u}_j \text{ for } j = 0, \ldots, N, \qquad \boldsymbol{w}_j \text{ for } j = 0, \ldots, (N-1) \tag{1a}$$

to minimize

$$J = \frac{1}{2}\left\{ \sum_{j=0}^{N-1} \left\| R_{w(j)}\boldsymbol{w}_j - z_{w(j)} \right\|^2 + \sum_{j=0}^{N} \left\| R_{u(j)}\boldsymbol{u}_j - z_{u(j)} \right\|^2 + \left\| \tilde{R}_0 \boldsymbol{x}_0 - \tilde{z}_0 \right\|^2 \right\} \tag{1b}$$

subject to

$$\boldsymbol{x}_{j+1} = \boldsymbol{f}_d(\boldsymbol{x}_j, \boldsymbol{w}_j, j) \qquad \text{for} \qquad j = 0, \ldots, (N-1) \tag{1c}$$

$$0 = \boldsymbol{h}(\boldsymbol{x}_j, \boldsymbol{y}_j, j) + \boldsymbol{u}_j \qquad \text{for} \qquad j = 0, \ldots, N \tag{1d}$$

In this model form, $\boldsymbol{x}_j$ is the state vector at sample time t_j, $\boldsymbol{w}_j$ is the process noise that acts from sample time t_j to t_{j+1}, $\boldsymbol{y}_j$ is the measurement vector at time t_j, and $\boldsymbol{u}_j$ is the residual measurement error at time t_j. The discrete-time dynamics are defined by the vector function $\boldsymbol{f}_d(\boldsymbol{x}_j, \boldsymbol{w}_j, j)$ in difference equation (1c). The implicit measurement model is defined by the function $\boldsymbol{h}(\boldsymbol{x}_j, \boldsymbol{y}_j, j)$ in Eq. (1d).

This smoother is a maximum likelihood estimator. The square nonsingular matrices $R_{w(j)}$, $R_{u(j)}$, and $\tilde{R}_0$ and the vectors $z_{w(j)}$, $z_{u(j)}$, and $\tilde{z}_0$ are used to define the least-squares cost function in Eq. (1b). These quantities also constitute a model of the a priori statistics of the process noise, the measurement error, and the initial state:

$$\boldsymbol{w}_j \sim N\left\{ R_{w(j)}^{-1} z_{w(j)},\, R_{w(j)}^{-1}\left[R_{w(j)}^{-1}\right]^T \right\} \tag{2a}$$

$$\boldsymbol{u}_j \sim N\left\{ R_{u(j)}^{-1} z_{u(j)},\, R_{u(j)}^{-1}\left[R_{u(j)}^{-1}\right]^T \right\} \tag{2b}$$

$$\boldsymbol{x}_0 \sim N\left\{ \tilde{R}_0^{-1} \tilde{z}_0,\, \tilde{R}_0^{-1}\left[\tilde{R}_0^{-1}\right]^T \right\} \tag{2c}$$

where the notation $\boldsymbol{q} \sim N\{\boldsymbol{v}, P\}$ indicates that $\boldsymbol{q}$ is a sample from a multivariate normal distribution whose mean is $\boldsymbol{v}$ and whose covariance is P. This problem model assumes that the random vectors $\boldsymbol{w}_j$, $\boldsymbol{u}_j$, and $\boldsymbol{x}_0$ are uncorrelated in time and uncorrelated with each other.

The dynamics function $\boldsymbol{f}_d(\boldsymbol{x}_j, \boldsymbol{w}_j, j)$ that appears in the discrete-time difference equation is defined via numerical solution of the following continuous-time initial value problem:

$$\dot{\bar{\boldsymbol{x}}}(t) = \boldsymbol{f}_c[\bar{\boldsymbol{x}}(t), \boldsymbol{w}_j, t] \qquad \text{for} \qquad t_j \leq t < t_{j+1} \tag{3a}$$

$$\bar{\boldsymbol{x}}(t_j) = \boldsymbol{x}_j \tag{3b}$$

The discrete-time function $\boldsymbol{f}_d(\boldsymbol{x}_j, \boldsymbol{w}_j, j)$ is defined as $\bar{\boldsymbol{x}}(t_{j+1})$, the solution of the initial value problem at time t_{j+1}. The Runge–Kutta technique is used to solve this initial value problem.

The CAPER attitude reconstruction problem can be modeled in this form. The function $\boldsymbol{f}_c[\bar{\boldsymbol{x}}(t), \boldsymbol{w}_j, j]$ is defined using a flexible-body attitude dynamics model and a colored noise process disturbance model. The elements of the vector function $\boldsymbol{h}(\boldsymbol{x}_j, \boldsymbol{y}_j, j)$ implicitly model the sun sensor, HCI, and magnetometer outputs. The matrices $R_{w(j)}$, $R_{u(j)}$, and $\tilde{R}_0$ and the vectors $z_{w(j)}$, $z_{u(j)}$, and $\tilde{z}_0$ are chosen partially based on the expected levels of random uncertainty and partially by tuning them to achieve a reasonable solution.

B. Smoother State Vector

CAPER's smoother state vector is

$$\boldsymbol{x} = [\boldsymbol{\omega}; \boldsymbol{q}_{\text{un}}; \alpha; \dot{\alpha}; \Delta I_{xx}; \Delta I_{xy}; \Delta I_{xz}; \Delta I_{yy}; \Delta I_{yz}; \boldsymbol{n}_{\text{in}}; \Delta h_{\text{HCI}}; \boldsymbol{b}_{\text{bias}}] \tag{4}$$

It has 21 elements. The first three elements are the vector $\boldsymbol{\omega}$, the inertial spin rate expressed in a coordinate system that is fixed to the main rigid part of CAPER. This coordinate system is depicted by the x, y, and z axes in Fig. 1. The nominal spin axis is the z axis. Throughout the remainder of this paper, this coordinate system will be referred to as the body-fixed or spacecraft-fixed coordinate system. The attitude quaternion $\boldsymbol{q}_{\text{un}}$ constitutes elements 4–7 of the state vector. It can be used to calculate the coordinate transformation from inertial coordinates to body-fixed coordinates $A_{\text{sc/in}}(\boldsymbol{q})$, where $\boldsymbol{q}$, the normalized quaternion, is computed as $\boldsymbol{q} = \boldsymbol{q}_{\text{un}}/\|\boldsymbol{q}_{\text{un}}\|$ because $\boldsymbol{q}_{\text{un}}$ may lose its normalization. The formula for $A_{\text{sc/in}}(\boldsymbol{q})$ is given in Ref. 1. This technique of using an unnormalized quaternion is one of several known ways to deal with difficulties that can arise when one includes an attitude quaternion in the state vector of a Kalman filter.[9]

The next two elements of the state vector come from the flexible-body part of the CAPER dynamics model. The eighth state vector element is α, the effective articulation angle of the flexible booms. The effective articulation is single-degree-of-freedom rotation about the $\hat{v}_{1b}$ axis; this axis is perpendicular to both the nominal boom direction and the nominal spin direction. The angle α and the unit vector $\hat{v}_{1b}$ are depicted on Fig. 1. The ninth state vector element is $\dot{\alpha}$.

The next five elements of the state vector, ΔI_{xx}, ΔI_{xy}, ΔI_{xz}, ΔI_{yy}, and ΔI_{yz}, are perturbations of inertia matrix elements for the main spacecraft body. There are perturbations for every independent element of the inertia matrix except for the nominal spin axis inertia.

The 15th–17th elements of the state vector constitute the random-walk disturbance torque vector $\boldsymbol{n}_{\text{in}}$. This disturbance vector is defined in inertial coordinates.

The remaining elements of the state vector are sensor biases. The HCI's trigger height bias Δh_{HCI} is the 18th element of the state vector. The magnetometer's bias vector $\boldsymbol{b}_{\text{bias}}$ constitutes the last three elements of the state vector.

C. Dynamics Model

The CAPER dynamics model consists of a set of differential equations that define the vector function $\boldsymbol{f}_c(\boldsymbol{x}, \boldsymbol{w}, t)$, which appears in Eq. (3a). Some of these equations are based on physics. Others constitute statistical models of random processes. The differential equation for the first three elements of $\dot{\boldsymbol{x}}$ is a generalization of Euler's rigid-body attitude dynamics equation. It includes the effects of flexible motion of the booms and equates the inertial rate of change of the angular momentum vector to the net external torque:

$$\dot{\boldsymbol{\omega}} = I_{\text{tot}}^{-1}\left\{ -2m_{\text{tip}} l_{\text{tip}}^2 \hat{\boldsymbol{v}}_{1b}\ddot{\alpha} - \dot{I}_{\text{tot}}\boldsymbol{\omega} - \boldsymbol{\omega} \times \left[I_{\text{tot}}\boldsymbol{\omega} + 2m_{\text{tip}} l_{\text{tip}}^2 \hat{\boldsymbol{v}}_{1b}\dot{\alpha} \right] + \boldsymbol{n}_{\text{gg}}(\boldsymbol{q}, \boldsymbol{r}_{\text{in}}, I_{\text{tot}}) + A_{\text{sc/in}}(\boldsymbol{q})\boldsymbol{n}_{\text{in}} + \boldsymbol{w}_{\text{sc}} \right\} \tag{5}$$

The matrix I_{tot} is the total inertia of the main rigid body plus the flexible booms. It is computed about the system center of mass and is expressed in body-fixed coordinates. The quantities m_{tip} and l_{tip} are, respectively, the tip mass and length of each of the flexible booms. The booms are assumed to be massless except for m_{tip}. The vector function $\boldsymbol{n}_{gg}(\boldsymbol{q}, \boldsymbol{r}_{\text{in}}, I_{\text{tot}})$ is the gravity gradient torque, which depends on the normalized attitude quaternion, the inertial position of the spacecraft in Earth-centered coordinates, $\boldsymbol{r}_{\text{in}}$, and the spacecraft total inertia. The vector $\boldsymbol{w}_{\text{sc}}$ is a white-noise process disturbance torque that is expressed in body-fixed axes.

The total spacecraft inertia can be computed by considering the geometry of Fig. 1. This computation uses unit vectors $\hat{\boldsymbol{v}}_{1b}$, $\hat{\boldsymbol{v}}_{2b}$, and $\hat{\boldsymbol{v}}_{3b}$. The direction $\hat{\boldsymbol{v}}_{2b}$ lies along the nominal boom direction. It is perpendicular to $\hat{\boldsymbol{v}}_{1b}$. The direction $\hat{\boldsymbol{v}}_{3b}$ is defined by the right-hand rule: $\hat{\boldsymbol{v}}_{3b} = \hat{\boldsymbol{v}}_{1b} \times \hat{\boldsymbol{v}}_{2b}$ Given these definitions, the total inertia is

$$I_{\text{tot}} = I_{\text{rb}} + \begin{bmatrix} \Delta I_{xx} & \Delta I_{xy} & \Delta I_{xz} \\ \Delta I_{xy} & \Delta I_{yy} & \Delta I_{yz} \\ \Delta I_{xz} & \Delta I_{yz} & 0 \end{bmatrix} + 2m_{\text{tip}} l_{\text{tip}}^2 \Big[\hat{\boldsymbol{v}}_{1b}\hat{\boldsymbol{v}}_{1b}^T + \sin^2\alpha\, \hat{\boldsymbol{v}}_{2b}\hat{\boldsymbol{v}}_{2b}^T$$
$$- \sin\alpha\cos\alpha \left(\hat{\boldsymbol{v}}_{2b}\hat{\boldsymbol{v}}_{3b}^T + \hat{\boldsymbol{v}}_{3b}\hat{\boldsymbol{v}}_{2b}^T \right) + \cos^2\alpha\, \hat{\boldsymbol{v}}_{3b}\hat{\boldsymbol{v}}_{3b}^T \Big] \tag{6}$$

where I_{rb} is the nominal inertia that the spacecraft would have if l_{tip} were zero. It is expressed in body-fixed coordinates about the system center of mass. The time derivative $\dot{I}_{\text{tot}}$ can be derived from Eq. (6) by using the chain rule and noting that α is the only time-varying quantity.

Equation (5) includes two random disturbance torque terms, $A_{\text{sc/in}}(\boldsymbol{q})\boldsymbol{n}_{\text{in}}$ and $\boldsymbol{w}_{\text{sc}}$. The first is a random-walk torque, and the second is a white-noise torque. Similar terms appear in the smoother model of Ref. 7. There are two main differences between these random torques and those of Ref. 7. The first is that the assumed intensities of these torques are much lower, relative to the spacecraft size, than those of Ref. 7. In other words, much less random torque is allowed as a way of fitting the measured CAPER data. The other difference is that Ref. 7 included a body-referenced random-walk torque, but the current model does not. Instead, it estimates inertia matrix perturbations ΔI_{xx}, ΔI_{xy}, ΔI_{xz}, ΔI_{yy}, and ΔI_{yz}. This alternative approach achieves similar effects, but in a way that is physically more realistic.

The attitude kinematics are governed by[1]

$$\dot{\boldsymbol{q}}_{\text{un}} = \frac{1}{2} \begin{bmatrix} 0 & \omega_z & -\omega_y & \omega_x \\ -\omega_z & 0 & \omega_x & \omega_y \\ \omega_y & -\omega_x & 0 & \omega_z \\ -\omega_x & -\omega_y & -\omega_z & 0 \end{bmatrix} \boldsymbol{q}_{\text{un}} \tag{7}$$

where ω_x, ω_y, and ω_z are the three body-fixed components of the spin rate vector $\boldsymbol{\omega}$.

The boom's rotational articulation motions are modeled by a second-order Markov process:

$$\ddot{\alpha} = -a_1\dot{\alpha} - a_2\alpha + w_\alpha \tag{8}$$

where a_1 and a_2 are constants that define the time correlation of the process and w_α is the white-noise input that drives the process. This model is not based on physics.

A physics-based model of the boom articulation motions has been considered during the development of this estimation system. It includes four flexible-body degrees of freedom and all of the usual physical interactions between the flexible booms and the main rocket's rigid body. Each boom is allowed to undergo first-mode bending in two planes. The resulting model has four boom flexure modes and rigid-body-type nutation and spin modes. The four flexible-body modes' oscillation frequencies are predicted to lie between 1.3 and 1.8 times the nutation frequency. These four modes are stable with predicted decay time constants on the order of 5 s or less. Thus, these flexible body modes decay to zero long before the start of the data interval.

This model's nutation mode is unstable. It includes slight boom articulations, which cause the instability. The articulations occur primarily in the plane that includes the nominal boom axis and the spin axis. The two booms oscillate 180 deg out of phase with each other. The model associated with Eq. (8) has been designed to capture this type of motion. It is possible to develop a physics-based version of Eq. (8), one that includes an actual boom stiffness and damping and the coupling effects of ω and $\dot{\omega}$ due to centrifugal, Coriolis, and angular acceleration effects. Such a model has not been used because the accuracy of the physics is poor due to large uncertainties in the booms' stiffness and damping. The Markov model allows the smoother to use the sensor data rather than physics to determine reasonable boom motions that can explain the growth in the nutation oscillations.

The dynamic models for the rates of the remaining elements of the state vector, elements 10–21, are as follows:

$$\Delta\dot{I}_{xx} = \Delta\dot{I}_{xy} = \Delta\dot{I}_{xz} = \Delta\dot{I}_{yy} = \Delta\dot{I}_{yz} = 0 \tag{9a}$$

$$\dot{\boldsymbol{n}}_{\text{in}} = \boldsymbol{w}_n \tag{9b}$$

$$\Delta\dot{h}_{\text{HCI}} = 0 \tag{9c}$$

$$\dot{\boldsymbol{b}}_{\text{bias}} = 0 \tag{9d}$$

In other words, all of the remaining state vector elements are modeled as being constants, except for $\boldsymbol{n}_{\text{in}}$. It is modeled as being a random-walk vector whose time evolution is driven by the white-noise process disturbance vector $\boldsymbol{w}_n$.

The process noise vector that appears in problem (1a–1d), $\boldsymbol{w}$, is seven dimensional and can be defined in terms of the white-noise process disturbances that appear in Eqs. (5), (8), and (9b):

$$\boldsymbol{w} = [w_\alpha; \boldsymbol{w}_n; \boldsymbol{w}_{\text{sc}}] \tag{10}$$

D. Attitude Sensor Models

The mathematical models of the attitude sensors are expressed in the functional form $\boldsymbol{h}(\boldsymbol{x}_j, \boldsymbol{y}_j, j)$ that appears in Eq. (1d). This function compares the measured attitude data $\boldsymbol{y}$ with a prediction that is based on the estimated state vector $\boldsymbol{x}$. Each element of $\boldsymbol{h}(\boldsymbol{x}_j, \boldsymbol{y}_j, j)$ measures the agreement between the model and the data. Perfect agreement yields $\boldsymbol{h}(\boldsymbol{x}_j, \boldsymbol{y}_j, j) = 0$ (Ref. 7).

1. Sun Sensor Model

The sun sensor is a slit-type device that digitizes a solar elevation angle whenever the sun passes through the plane of its slit. It produces a measured sun vector in spacecraft coordinates $\hat{\boldsymbol{s}}_{\text{sc(meas)}}$ once per spin period. This sample period is 5 s at the beginning of the flight, but it lengthens throughout the flight as the spin rate decays. One can determine a modeled value of the sun unit vector in inertial coordinates $\hat{\boldsymbol{s}}_{\text{in(eph)}}$ from the solar ephemeris. Given these quantities, the sun sensor elements of $\boldsymbol{h}(\boldsymbol{x}_j, \boldsymbol{y}_j, j)$ are

$$\boldsymbol{h}_{\text{ss}}(\boldsymbol{x}_j, \boldsymbol{y}_j, j) = \hat{\boldsymbol{s}}_{\text{sc(meas)}} \times \left[A_{\text{sc/in}}(\boldsymbol{q})\, \hat{\boldsymbol{s}}_{\text{in(eph)}} \right] \tag{11}$$

This vector defines the rotation needed to align the measured and modeled sun directions.

The expected raw accuracy of CAPER's sun sensor is about 1 deg. Its elevation digitization resolution is 2 deg, but the pixel intensity data admit finer interpolation. The sensor is uncalibrated, which is why its accuracy is so low. Two additional error sources are the Earth's albedo and the mounting alignment tolerance, which is on the order of 1 deg. The net measurement accuracy of this instrument has been modeled as being about 2–3 deg.

2. HCI Model

The HCI is a narrow field-of-view telescope whose line of sight is fixed in the body frame. It measures the total received intensity in a radiation band that is emitted by atmospheric CO_2. Body axes rotation causes the telescope line of sight to scan, and the detector's output undergoes sharp changes when it scans through the point of tangency to an ellipsoid that is approximately 40 km above the surface of the oblate Earth. The HCI's output data are the times of these abrupt changes in the signal level. These outputs come twice per spin period (i.e., twice every 5 s at the start of the flight), but more slowly near the end.

The HCI's $\boldsymbol{h}(\boldsymbol{x}_j, \boldsymbol{y}_j, j)$ element is defined by the tangency condition. The mathematical model for the tangency condition uses a weighting matrix to deal with the Earth's oblateness: $P = \mathrm{diag}\{1, 1, [(r_{\mathrm{eq}} + 40\,\mathrm{km} + \Delta h_{\mathrm{HCI}})/(r_{\mathrm{po}} + 40\,\mathrm{km} + \Delta h_{\mathrm{HCI}})]\}$, where r_{eq} is the equatorial Earth radius and r_{po} is the polar Earth radius. The model also uses two vectors that are weighted by this matrix: $\boldsymbol{r}_w = P\boldsymbol{r}_{\mathrm{in}}$, and $\boldsymbol{v}_w = PA^T_{\mathrm{sc/in}}(\boldsymbol{q})\hat{\boldsymbol{v}}_{\mathrm{sc(HCI)}}$, where $\hat{\boldsymbol{v}}_{\mathrm{sc(HCI)}}$ is the unit vector that points along the HCI line of sight in body-fixed coordinates. Recall that $\boldsymbol{r}_{\mathrm{in}}$ is the inertial spacecraft position relative to the Earth, which is supplied by an onboard global positioning system receiver. Given these definitions, the HCI part of the $\boldsymbol{h}(\boldsymbol{x}_j, \boldsymbol{y}_j, j)$ function is

$$\begin{aligned}\boldsymbol{h}_{\mathrm{HCI}}(\boldsymbol{x}_j, \boldsymbol{y}_j, j) &= (r_{\mathrm{eq}} + 40\,\mathrm{km} + \Delta h_{\mathrm{HCI}})^2 \\ &\quad - \boldsymbol{r}_w^T\left(I - \boldsymbol{v}_w\boldsymbol{v}_w^T \big/ \boldsymbol{v}_w^T\boldsymbol{v}_w\right)\boldsymbol{r}_w\end{aligned} \tag{12}$$

This formula requires that $\boldsymbol{v}_w^T\boldsymbol{r}_w < 0$, which is true for reasonable levels of measurement error.

The accuracy of this attitude measurement depends on the uncertainty in the trigger height. Trigger height uncertainty can result from two sources. One is a height variation of the Earth's atmosphere as a function of the season and the local time of the point of tangency.[10] Additional uncertainty comes from the way that the detector's raw intensity data get translated into a time of tangency. A simple approach has been used: Tangency is considered to occur when the detected intensity reaches 50% of its maximum value. Data analysis shows that the resulting trigger height random errors may be as large as 70 km. This error magnitude translates into a 0.9-deg attitude measurement error at CAPER's 1360-km apogee altitude and a 1.7-deg error at the lowest altitude of interest, 420 km.

3. *Magnetometer Model*

The magnetometer is a three-axis flux gate device. Its output is the measured magnetic field vector in spacecraft coordinates $\boldsymbol{b}_{\mathrm{sc(mes)}}$ (tesla). It is sampled at a nominal frequency of 4 Hz. It can be used as an attitude reference by comparing it with the known inertial magnetic field, which comes from a model.[1,11] If the modeled inertial field is $\boldsymbol{b}_{\mathrm{in(mod)}}(\boldsymbol{r}_{\mathrm{in}}, t)$, then the mathematical model of the magnetometer part of $\boldsymbol{h}(\boldsymbol{x}_j, \boldsymbol{y}_j, j)$ is

$$\boldsymbol{h}_{\mathrm{MAG}}(\boldsymbol{x}_j, \boldsymbol{y}_j, j) = \left(\boldsymbol{b}_{\mathrm{sc(mes)}} - \boldsymbol{b}_{\mathrm{bias}}\right) - A_{\mathrm{sc/in}}(\boldsymbol{q})\,\boldsymbol{b}_{\mathrm{in(mod)}}(\boldsymbol{r}_{\mathrm{in}}, t) \tag{13}$$

This error is a simple difference between the modeled field and the measured field, in spacecraft coordinates, after the estimated bias states have been subtracted from the measured field.

There are various sources of error in the magnetometer data. Errors from spacecraft-generated fields are low due to the sensor's location on a boom. Similarly, errors due to resolution and miscalibration are all low, under 6 nT. The dominant errors come from the sensor's loose orthogonality and alignment requirements, only ±1 deg, from uncertainty in the Earth's magnetic field model, and from disturbances to the field. These errors add about 1000 nT to the measurement uncertainty. For the field magnitude range experienced during the flight, 32,000–46,000 nT, these error levels translate into an attitude measurement uncertainty on the order of from 1 to 2 deg.

E. Miscellaneous Smoother Details for CAPER Application

1. *Attitude and Rate Initialization*

Proper initialization of the filter/smoother's attitude and attitude rate is important due to the nonlinear nature of the extended estimation algorithm of Ref. 7. A poor initialization could lead to divergence during the forward filtering pass.

Initialization is accomplished as follows: First, the magnetic field time history is used to estimate the initial spin vector in spacecraft coordinates. The procedure neglects the slow inertial time variations of the magnetic field direction that are caused by the rocket's motion along its trajectory. This leads to the relationship $\dot{\hat{\boldsymbol{b}}}_{\mathrm{sc}} = -\boldsymbol{\omega} \times \hat{\boldsymbol{b}}_{\mathrm{sc}} = \hat{\boldsymbol{b}}_{\mathrm{sc}} \times \boldsymbol{\omega}$, where $\hat{\boldsymbol{b}}_{\mathrm{sc}}$ is the unit direction vector of the Earth's magnetic field as measured in spacecraft coordinates. The vector $\hat{\boldsymbol{b}}_{\mathrm{sc}}(t)$ is available from the magnetometer (if one neglects biases), and $\dot{\hat{\boldsymbol{b}}}_{\mathrm{sc}}(t)$ can be derived from $\hat{\boldsymbol{b}}_{\mathrm{sc}}(t)$. If one uses this relationship at two different times that are approximately a quarter of a spin period apart, then one can derive a set of six linear equations in the three unknown elements of $\boldsymbol{\omega}$. If the spin vector is not aligned with the field vector, then four of these six equations are linearly independent, and this overdetermined set of equations can be solved in a least-squares sense to estimate $\boldsymbol{\omega}$. The spin and field vectors are not aligned for the initial part of the CAPER data set; thus, this technique works well.

Once the spin vector is known, the only remaining task is to estimate the initial attitude quaternion $\boldsymbol{q}_{\mathrm{un}}$. It is estimated by using measured and reference values of two noncollinear unit direction vectors, the normalized magnetic field vector and the sun direction vector. The initialization is carried out at an instant when both of these measurements are available.

All other elements of the state vector are assigned a priori values of zero at the initial time of the filter/smoother data interval, t_0. Therefore, only the first seven elements of the vector $\tilde{z}_0$ are nonzero because these are the elements associated with the spin rate and the attitude.

2. *Data Validation*

Two simple checks have been performed to validate the sun sensor and magnetometer data. One quantity that has been checked is the magnitude of the measured magnetic field. It has been compared to the magnitude of the modeled field. The maximum absolute difference between measured and modeled field magnitudes is 1530 nT, and the maximum percentage difference is 4.2%. These values occur when there is no magnetometer bias estimation. With bias estimation, the maximum respective differences are 600 nT and 1.8%. This low error level indicates that the magnetometer measurements are reliable.

The other data check has compared the measured and modeled values of the angle between the sun vector and the magnetic field vector. With compensation for magnetometer biases, the maximum angular discrepancy between the measurements and the model is 2.8 deg. This level of agreement is acceptable given CAPER's required attitude accuracy. It indicates that the attitude accuracy from the sun sensor, from the magnetometer, or from both is about 2–3 deg.

3. *Data Editing*

Some of the sun sensor and HCI data seemed to be invalid. Suspicious data points exhibited large smoothed measurement residuals $\boldsymbol{u}_j$. All such data points have been discarded. In total, 9 out of 235 HCI data points have been discarded, as have 6 out of 98 sun sensor data points. All of the edited sun sensor points occurred after apogee, when CAPER's coning half-angle had grown to more than 55 deg. At such large coning half-angles the sun sensor sometimes had a problem with a high-reading/low-reading ambiguity in its output digitization map. The edited HCI data mostly occurred well before apogee. It is not clear what might have contributed to errors in these data points, except that there may have been a breakdown in the algorithm for deducing horizon crossing times from the recorded radiation intensity time history.

4. *Sensor Alignment Estimation*

Sometimes attitude determination filters or smoothers are used to estimate sensor misalignments, as in Ref. 7. In the present case, it was not considered to be worthwhile to try to estimate the relative misalignment between the sun sensor and the magnetometer. This decision was made because it is difficult, perhaps not even possible, to estimate this misalignment accurately.

The one misalignment that has been estimated is that of the HCI bore sight vector as measured in spacecraft coordinates $\hat{\boldsymbol{v}}_{\mathrm{sc(HCI)}}$. There were early indications that the reported direction of this vector could be in error by as much as 2 or 3 deg. The misalignment of this vector has been estimated by using a batch process. The batch process makes use of the basic smoother. The smoother is run using a large assumed HCI measurement uncertainty, which causes the algorithm to ignore the HCI data and to use only magnetometer and sun sensor data to form its attitude estimate. This attitude estimate is then used to calculate HCI measurement errors $\boldsymbol{h}_{\mathrm{HCI}}(\boldsymbol{x}_j, \boldsymbol{y}_j, j)$. The vector $\hat{\boldsymbol{v}}_{\mathrm{sc(HCI)}}$ is then perturbed in two orthogonal directions, and the smoother is run two more times to determine the effect of $\hat{\boldsymbol{v}}_{\mathrm{sc(HCI)}}$ perturbations on the HCI measurement errors. Finally, this linearized model is used in a batch least-squares calculation to correct $\hat{\boldsymbol{v}}_{\mathrm{sc(HCI)}}$ in such a way that the corrected vector yields the minimum mean square HCI measurement error. This procedure results in a 2.1 deg correction to the direction of $\hat{\boldsymbol{v}}_{\mathrm{sc(HCI)}}$.

5. *Iterative Inertia Matrix Estimation and the Final Estimate*

The smoother assumes nominal values for the six elements of I_{rb}, and it estimates perturbations to five of these parameters. The smoother's performance can be slightly influenced by large errors in the initial nominal values of inertia parameters. One influence comes from the nonlinearity of the smoother, and the other influence comes from the need to assign some noninfinite initial level of uncertainty to the five estimated perturbations.

An iterative inertia estimation process has been employed to minimize the impact of initial errors in the nominal values. This iterative process is simple: The smoother is first run using design values for the nominal inertias. The next time the smoother is run, it uses new nominal values, the preceding nominal values plus the estimated perturbations from the preceding smoother run. This process has been iterated only two times, after which the estimated perturbations are all less than 1% of the system's maximum principal inertia.

The final estimates of the nominal total system principal inertias are 211.73, 190.84, and 18.72 $\mathrm{kg \cdot m^2}$. These inertias include the booms, whose properties are $l_{\mathrm{tip}} = 3.24$ m and $m_{\mathrm{tip}} = 0.4288$ kg. The initial spin rate is 1.35 rad/s, which gives rise to a rigid-body nutation frequency of 1.23 rad/s. Toward the end of the flight, the spin rate slows to 0.35 rad/s, which corresponds to a nutation frequency of 0.32 rad/s.

6. *Smoother Tuning*

The smoother gets tuned via selection of quantities that model various a priori error statistics. The matrix $\tilde{R}_0$ is initialized to reflect the estimation error covariances for the a priori initial state estimate, $\tilde{\boldsymbol{x}}_0 = \tilde{R}_0^{-1}\tilde{\boldsymbol{z}}_0$. Except for a modification in the quaternion terms, $\tilde{R}_0$ is a diagonal matrix. Each diagonal element is of the form $1/\sigma$, where σ is an a priori state estimation error standard deviation. The a priori standard deviations are 16 deg/s for each element of the spin vector $\boldsymbol{\omega}$ (20% of the initial spin rate); 15 deg for each independent direction of attitude uncertainty; 10 deg for the initial α uncertainty; 20 deg/s for the initial $\dot{\alpha}$ uncertainty; 30 $\mathrm{kg \cdot m^2}$ for the initial ΔI_{xx} and ΔI_{yy} uncertainties; 10 $\mathrm{kg \cdot m^2}$ for the initial ΔI_{xy}, ΔI_{xz}, and ΔI_{yz} uncertainties; 0.0006 $\mathrm{N \cdot m}$ for each element of the inertial random-walk disturbance vector $\boldsymbol{n}_{\mathrm{in}}$; 20,000 m for the HCI trigger height bias Δh_{HCI}; and 3000 nT for each element of the magnetometer bias vector $\boldsymbol{b}_{\mathrm{bias}}$. With the exception of the random-walk disturbance torques, these a priori standard deviations have been chosen to be as large as seemed practical. This approach minimizes the initializations' effects on the final smoother solution. The possibility of filter/smoother divergence is what places practical maximum limitations on the sizes of the a priori initial standard deviations.

The measurement noise statistics have been modeled as follows: $z_{u(j)}$ has been set equal to zero for all sample times because the measurement errors are assumed to have zero mean. The measurement error standard deviations are used to form the elements of the diagonal matrix $R_{u(j)}$. As with $\tilde{R}_0$, if σ is the standard deviation of a particular measurement, then $1/\sigma$ is the corresponding diagonal element of $R_{u(j)}$. The sun sensor measurement standard deviation was set to 5 deg per axis, the HCI σ value was set to 132,000 m, and the magnetometer's random error component was modeled as having a standard deviation of 3000 nT per axis.

The process noise statistical model defines the $z_{w(j)}$ vector, the $R_{w(j)}$ matrix, and the values of a_1 and a_2 in the Markov model of the boom articulations. The vector $z_{w(j)}$ has been set equal to zero, and the matrix $R_{w(j)}$ has been defined as follows:

$$\begin{aligned} R_{w(j)} = \mathrm{diag}(&1/\sigma_{w\alpha}, 1/\sigma_{wn}, 1/\sigma_{wn}, 1/\sigma_{wn}, \\ &1/\sigma_{wsc}, 1/\sigma_{wsc} 1/\sigma_{wsc})\sqrt{t_{j+1} - t_j} \end{aligned} \tag{14}$$

where $\sigma_{w\alpha} = 48$ $\mathrm{deg/s^{1.5}}$, $\sigma_{wn} = 6 \times 10^{-5}$ $\mathrm{N \cdot m/s^{0.5}}$, and $\sigma_{wsc} = 1.5 \times 10^{-3}$ $\mathrm{N \cdot m \cdot s^{0.5}}$.

The Markov process in Eq. (8) is assigned an undamped natural frequency of 2 rad/s and a damping ratio of 0.7071. Therefore, $a_1 = 2.8284\ \mathrm{s^{-1}}$ and $a_2 = 4\ \mathrm{s^{-2}}$.

7. *Smoother Tuning Process*

The smoother requires a certain amount of tuning to arrive at the numbers given in the preceding section. The important tuning parameters are the sensor accuracies that appear in inverse form in the $R_{u(j)}$ matrix and the process noise intensities whose inverses form the diagonal elements of $R_{w(j)}$. The magnetometer and sun sensor error standard deviations are chosen to be about a factor of two larger than the error levels noted in the data validation section of this paper. The parameters of the boom articulation Markov model in Eq. (8), a_1, a_2, and $\sigma_{w\alpha}$, are chosen to give a bandwidth that is slightly higher than the nutation frequency and a steady-state α standard deviation that is about four times larger than what is expected based on physical models. The remaining tuning parameters, the HCI measurement error standard deviation and the process noise intensities for the white-noise and random-walk torques, are chosen by trial-and-error runs of the smoother.

The tuning process starts with a larger HCI measurement error standard deviation and larger process noise intensities than were reported earlier. The initial trial value of the HCI noise standard deviation is 1.3 times the final best-case value, and the initial trial values of the process noise intensities σ_{wn} and σ_{wsc} are 33 times larger than the final values.

Smoothing runs are attempted with successively lower values of these noise standard deviations until the final best-case values are determined. The goal is to use the lowest possible values for the HCI errors and the random torque intensities because it is believed that these error sources should be small. At some point, the smoother begins to exhibit poor performance when smaller values for these noise intensities are used. This poor performance is evident in the smoother's measurement error estimates: Their time histories exhibit large spikes. The final best-case tunings of these quantities are selected as the smallest values that do not cause obvious large spikes in the smoothed measurement errors.

III. Attitude Determination Results

The smoother of Sec. II has been run on the actual data from the CAPER mission. Several different runs have been made. Also, comparison runs have been made using a smoother that employs only a rigid-body model and larger disturbance torques, like that of Ref. 7. Results of these runs are presented in this section.

A. Best-Case Smoother Performance

This subsection discusses the smoother's performance under the best possible tunings, those that have been presented at the end of Sec. II.

The first plots to consider are those of the smoothed residual measurement errors. These are the values of the elements of $\boldsymbol{h}(\boldsymbol{x}_j, \boldsymbol{y}_j, j)$, but rescaled into equivalent angular units. The sun sensor error time histories are plotted on the top plot of Fig. 2, the magnetometer

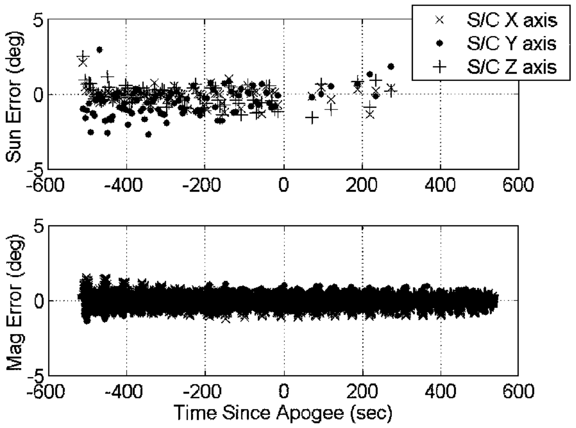

Fig. 2 Smoothed sun sensor and magnetometer residual measurement error time histories.

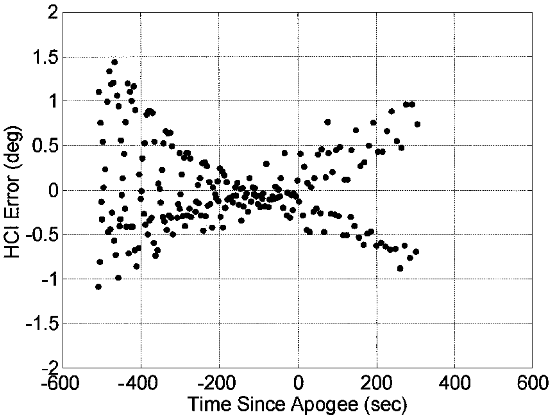

Fig. 3 Smoothed HCI residual measurement error time history.

errors appear on the bottom plot, and the HCI errors are presented in Fig. 3. The sun sensor and magnetometer errors are both given in spacecraft coordinates.

There are several significant points to note about the smoothed measurement errors. First, there are no sun sensor or HCI measurement errors for the last 200 s of the data interval, that is, from 300 to 500 s after apogee. The large final coning angles of CAPER caused this loss of data. Second, all of these errors are of a reasonable size based on the modeled statistics. The sun sensor errors are all less than 3 deg, and most are less than 2.5 deg. The magnetometer errors are all less than 1.6 deg, and the HCI errors are all less than 1.5 deg. The third point is that the errors appear to have some correlation. The most striking correlations appear in the HCI errors of Fig. 3. Roughly speaking, the points of Fig. 3 can be described as forming a flattened X. The upper-left to lower-right stroke of the X is formed primarily by in crossings (i.e., by space-to-Earth scans of the horizon telescope), and the lower-left to upper-right branch of the X is formed primarily by out crossings (Earth-to-space scans). The magnetometer errors show a different kind of correlation. Although not obvious on the scale of the plot due to the density of the points, there is a periodicity to the errors that corresponds to the body-axis nutation period.

It is not clear why there are correlations in the smoothed measurement errors. The theory of smoothers says that there should be no such correlation if the system is perfectly modeled and if the error sources are truly random. Obviously, some of these assumptions are violated by the system. One possible source of the systematic errors is the loose orthogonality specification on the magnetometer axes and the lack of sun sensor calibration. HCI misalignment cannot explain the HCI innovations, however, because the HCI alignment has been estimated by minimizing these residual errors, as explained in Sec. II. Despite these problems with the residuals, this performance is probably adequate for the mission at hand. In any case, the attitude accuracy has been checked by an independent measurement, as will be discussed hereafter.

The estimated spin vector time history for this case is shown in Fig. 4. The spin vector starts out pointed mostly along the z axis, which is the nominal spin axis. As time progresses, the amplitude of the (ω_x, ω_y) nutation grows, and the magnitude of ω_z decreases. At the end of the mission, the spin vector is about 20 deg away from the z axis. More importantly, the angular momentum vector is more than 75 deg away from the z axis at the end of the mission. This latter angle is the observed coning half-angle of the system, which means that CAPER was in a flat spin at the end of its flight.

The boom articulation angle time history $\alpha(t)$ is shown in Fig. 5. This plot is roughly consistent with the response that is predicted by a physics-based model of this system, that is, by the model that is described in the paragraphs that follow Eq. (8) in Sec. II. The primary boom response is an oscillation at the body-axes nutation frequency of the spin vector, and the magnitude is between 4 and 10 deg peak-to-peak. The response lags behind the forcing that arises due to centrifugal effects and angular acceleration. This lag is what causes energy loss and the resultant growth of the nutation amplitude.

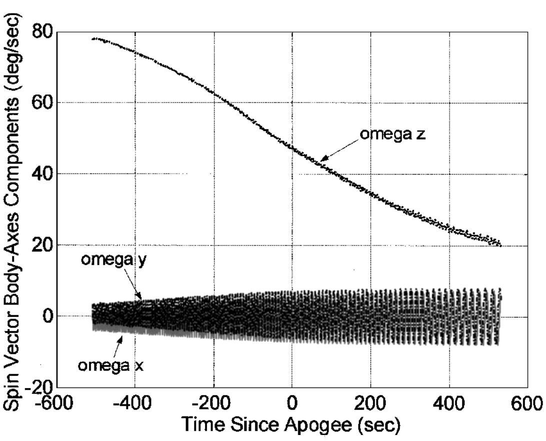

Fig. 4 Nominal smoother's estimated spin vector time history, $\omega(t)$.

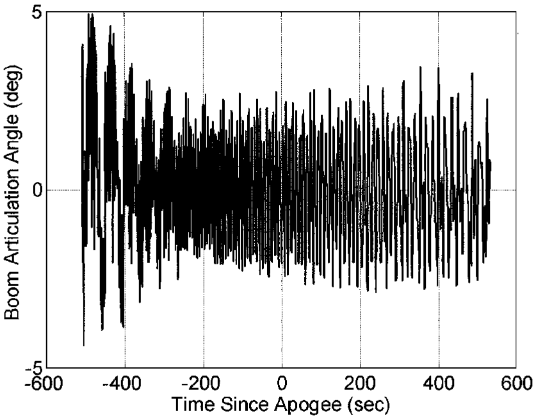

Fig. 5 Boom articulation angle time history $\alpha(t)$ for the nominal smoother.

There is one strange part of Fig. 5, namely, the amplitude beats that occur during the first 250 s of the data interval. There is no obvious explanation for these. They correspond to small transient energy oscillations in the system that seem to be nonphysical. These beats may be caused by systematic measurement errors. The resultant anomalous motions are not large; thus, it is reasonable to ignore this problem.

The total external torque for this case is relatively low. The maximum magnitude of the total estimated random torque, $\max\|A_{\mathrm{sc/in}}(\boldsymbol{q})\boldsymbol{n}_{\mathrm{in}} + \boldsymbol{w}_{\mathrm{sc}}\|$, is 0.0011 N · m. Although small, this value is at least one order of magnitude larger than the maximum expected disturbances from drag and solar radiation pressure. An attempt has been made to model the external torque by estimating a residual spacecraft magnetic dipole moment, but such a model explains little of the observed disturbances. The only possible explanation for these residual torques is an unknown modeling error either in the dynamics or in the sensors.

The estimated torques do not cause the estimated angular momentum vector to drift much in inertial space. The magnitude of the angular momentum stays within 2.3% of its initial value, and the inertial orientation drifts by less than 1 deg. An important feature of the inertial angular momentum estimate is its orientation drift during the last 200 s of the data interval. As shown in Figs. 2 and 3, there are no sun sensor or HCI measurements during this time interval. Therefore, the system is not totally observable because it has only one useable attitude reference, the magnetic field. This implies that the smoother's attitude estimate during the last 200 s is, in part, an extrapolation from earlier sun sensor and horizon sensor measurements. The angular momentum vector drifts by only 0.2 deg during this final phase, which implies that the extrapolation is reasonably accurate.

The nominal smoother's estimated total kinetic energy time history is shown in Fig. 6. As expected, this plot shows a dramatic

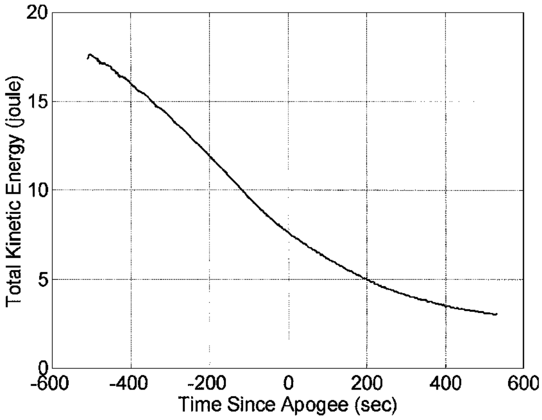

Fig. 6 Estimated total kinetic energy time history for the nominal smoother.

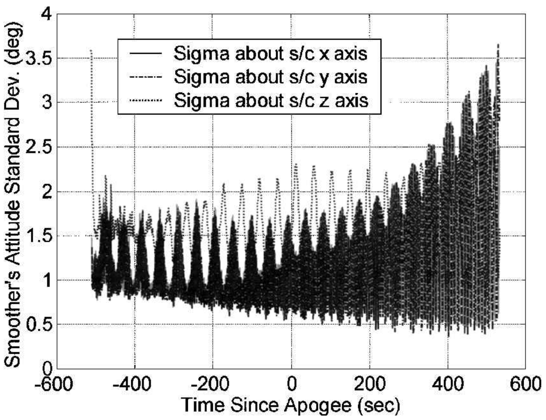

Fig. 7 Smoother's computed attitude error standard deviation time histories.

loss of energy as the flight progresses. This loss is associated with nutation growth for a minor-axis spinner. It is caused by damping in the nutation mode's boom articulation oscillations.

Figure 6 shows a slight kinetic energy increase for the first 8 s of the data interval. This increase is nonphysical. Note that this small wrinkle in the plot occurs at the same time that an anomalous boom articulation angle beat appears on Fig. 5. It is believed that both of these responses are the results of the same systematic modeling error.

Time histories of the smoother's computed attitude error standard deviations are plotted in Fig. 7. These are based on the smoother tuning parameters that have been presented in Sec. II. These are the accuracies that the smoother thinks it has achieved. The actual accuracies will differ from these values due to various types of modeling error. Nevertheless, these time histories give a good indication of how the smoother is performing. They show that it maintains reasonable observability during most of the data interval, as evidenced by the nearly constant level of the plots from about -500 to $+200$ s. For $t > 200$ s, the x-axis and y-axis standard deviations drift higher due to the lack of sun sensor and HCI data, but this growth in the attitude uncertainty is not rapid enough to cause serious accuracy problems before the end of the mission.

B. Attitude Checks

These results have been checked using the ***q*** method, which computes point attitude solutions.[12] The ***q*** method has been applied whenever there are simultaneous sun sensor and magnetometer measurements. These two vector measurements have been weighted equally in the point solutions. This check yields a 4-deg peak attitude difference between the ***q*** method point solutions and the smoother's solution.

The smoother's attitude estimates have been partially verified using independent data. This data comes from electric field probes that are mounted at the ends of the booms. These probes are known to experience voltage spikes when they pass through the rocket body's solar shadow. These shadowing times can be predicted based on the main spacecraft body's geometry and the smoother's attitude estimate. These predictions have been generated, and they have been compared to the times of the actual spikes in the probe voltage time histories. There are 161 observable spikes in the data, and 136 of these match with predicted spikes. The other 25 data spikes are not predicted at all, probably due to approximation errors of the geometric shading model that has been used to generate the predictions. The relevant spikes in the voltage time histories have been found to agree with the 136 predicted spikes to within 0.14 s. If one multiplies the estimated spin rate by these timing errors, then they yield a maximum spacecraft orientation error of 3.9 deg. These shadowing data extend all of the way to the end of the flight. Therefore, these positive results verify that the smoother yields a reasonable attitude estimate even when sun sensor and HCI data are no longer available.

This shadowing result is better than what is implied by the smoother's computed standard deviations. The 3.9-deg shadowing error is a peak value. Figure 7 shows smoother standard deviations as large as 3.6 deg. Peak errors are typically about three times larger than standard deviations. Thus, the smoother's computed upper bound on the peak error is 10.8 deg.

This apparent conservatism of the smoother's computed variances is consistent with a comparison between the smoother's assumed measurement error standard deviations and the actual computed measurement residuals, as shown in Figs. 2 and 3. The smoother's modeled measurement error standard deviations are significantly larger than the standard deviations of the computed measurement residuals (5.2 times larger for the sun sensor, 4.5 times larger for the HCI, and 13.8 times larger for the magnetometer). This conservatism in the smoother's tuning translates almost directly into a conservatism in its computed covariances.

C. Conjecture About Factors that Limit the Attitude Accuracy

It is believed that the limiting factors in the accuracy of this example come from measurement errors in CAPER's attitude sensors. As seen in Figs. 2 and 3 and in the independent data consistency checks, the raw attitude measurement errors are on the order of 1–3 deg. The shading check demonstrates that the attitude solution has about the same level of accuracy. Furthermore, there seem to be systematic effects in the measurement errors. These systematic effects probably keep the smoother from using its averaging capabilities to achieve results that are more accurate than the raw sensor data. Therefore, it is believed that the accuracy of this attitude solution technique could be significantly improved if better sensors were available.

D. Comparison with a Rigid-Body Based Smoother

The present results have been compared with a smoother like that of Ref. 7. It uses a rigid-body model of the spacecraft, and it allows larger disturbance torque estimates to try to account for various sources of modeling error, including flexible-body effects. It includes random-walk torques both in inertial axes and in body axes. The inertial torques account for any unmodeled precession of the angular momentum vector, and the body-axis torques account for effects such as principal axis modeling errors.

The CAPER results for this rigid-body type smoother are problematic. The estimated random torques are large. They vary between 0.3 and 0.4 N · m for most of the run, and they spike up as high as 20 and 28 N · m during two anomalous parts of the smoothed solution. Even without the anomalous portions, the average estimated torques are about 300 times larger than for the smoother that uses a flexible-body model. Such large disturbance torques are totally inconsistent with the physics of the system.

Figure 8 gives a summary comparison between the two attitude estimation algorithms. It plots the total angular discrepancy between the flexible-body smoother's attitude estimate and that of the rigid-body smoother. The two smoothers agree fairly well up to about 100 s after apogee. Full three axis attitude measurement data are available during this time period, and the coning half angle is less than 60 deg. The two attitude estimates stay within 2 deg of each other during this period, except for a small initial spike of 4.2 deg.

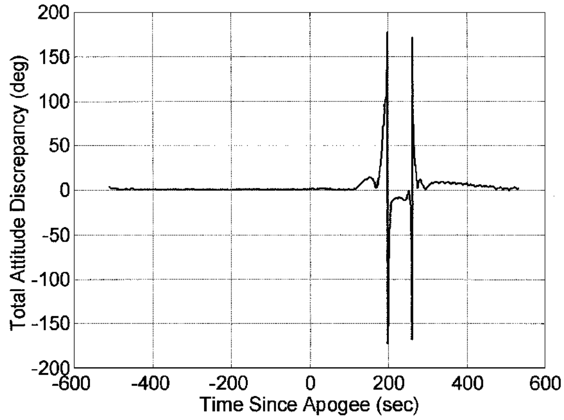

Fig. 8 Time history of attitude discrepancy between flexible-body and rigid-body smoothers.

The rigid-body-based smoother experiences serious problems starting at about 100 s after apogee. These are evidenced by large residual measurement errors and by spikes in the estimated spin vector. Figure 8 shows corresponding spikes in the attitude discrepancy between the two smoothers. These are caused by erroneous 360-deg rotations of the rigid-body smoother's attitude estimate. The rigid-body smoother has problems in dealing with a sparse set of measurement data, a large coning half-angle, or both.

IV. Conclusions

This paper describes an attitude reconstruction smoother that has been applied to the CAPER mission. The achieved accuracy of the smoother is estimated to be about 4 deg per axis. This estimate is based on the level of the smoothed residual attitude measurement errors and on independent data: the solar shading times for boom-mounted electric field probes.

The smoother has two new features that are important to its success. First, it estimates corrections to five of the six independent elements of the inertia matrix of the main spacecraft body. Second, it explicitly incorporates a simple model of the dominant flexible-body motion of a pair of elastic booms. The energy loss in the boom deflections causes nutation growth because CAPER is a minor-axis spinner. The estimated coning half angle grows from 20 deg at the start of the mission to over 75 deg by the end of the flight. The flexible-body model allows the smoother to reconstruct attitude accurately at the end of the flight despite the fact that CAPER's flat terminal spin causes some of the sensors to stop returning data.

Acknowledgments

This work was supported in part by NASA Grant NAG5-5079, Cleft Accelerated Plasma Experimental Rocket. The payload and rocket were designed and built at the NASA Goddard Space Flight Center, Wallops Flight Facility.

References

[1] Wertz, J. R. (ed.), *Spacecraft Attitude Determination and Control*, D. Reidel, Boston, 1978, pp. 414, 501, 502, 512, 779–786.

[2] Levinson, D. A., and Kane, T. R., "Spin Stability of a Satellite Equipped with Four Booms," *Journal of Spacecraft and Rockets*, Vol. 13, No. 4, 1976, pp. 208–213.

[3] Lefferts, E. J., Markley, F. L., and Shuster, M. D., "Kalman Filtering for Spacecraft Attitude Estimation," *Journal of Guidance, Control, and Dynamics*, Vol. 5, No. 5, 1982, pp. 417–429.

[4] Rupp, T., and Schneiders, G., "High-Accuracy Attitude Determination for the X-Ray Satellite ROSAT," *Journal of Guidance, Control, and Dynamics*, Vol. 15, No. 3, 1992, pp. 554–561.

[5] Psiaki, M. L., Martel, F., and Pal, P. K., "Three-Axis Attitude Determination via Kalman Filtering of Magnetometer Data," *Journal of Guidance, Control, and Dynamics*, Vol. 13, No. 3, 1990, pp. 506–514.

[6] Axelrad, P., and Ward, L. M., "Spacecraft Attitude Estimation Using the Global Positioning System: Methodology and Results for RADCAL," *Journal of Guidance, Control, and Dynamics*, Vol. 19, No. 6, 1996, pp. 1201–1209.

[7] Psiaki, M. L., Theiler, J., Bloch, J., Ryan, S., Dill, R. W., and Warner, R. E., "ALEXIS Spacecraft Attitude Reconstruction with Thermal/Flexible Motions Due to Launch Damage," *Journal of Guidance, Control, and Dynamics*, Vol. 20, No. 5, 1997, pp. 1033–1041.

[8] Bierman, G. J., *Factorization Methods for Discrete Sequential Estimation*, Academic Press, New York, 1977, pp. 69–76, 115–122, 214–217.

[9] Bar-Itzhack, I. Y., Deutschmann, J., and Markley, F. L., "Quaternion Normalization in Additive EKF for Spacecraft Attitude Determination," *Proceedings of the AIAA Guidance, Navigation, and Control Conference*, Vol. 2, AIAA, Washington, DC, 1991, pp. 908–916.

[10] Cowley, J. R., "Horizon Sensor Trigger Altitudes Derived from Apparent Pitch Variations of the Solar Mesosphere Explorer," American Astronautical Society, Paper AAS-87-493, 1987.

[11] "DGRF/IGRF Geomagnetic Field Model 1945–2000 and Related Parameters," National Space Science Data Center, NASA Goddard Space Flight Center, 1999, URL:http://nssdc.gsfc.nasa.gov/space/model/models/igrf.html [cited 24 November 2001].

[12] Shuster, M. D., and Oh, S. D., "Three-Axis Attitude Determination from Vector Observations," *Journal of Guidance and Control*, Vol. 4, No. 1, 1981, pp. 70–77.